

# Realizing Direct Hot-Electron Transfer from Metal Nanoparticles to Per- and polyfluoroalkyl Substances

P. K. Verma,<sup>†</sup> Samir Kumar Nayak,<sup>‡</sup> Khushboo Bhardwaj,<sup>‡</sup> and Sharma S. R. K. C. Yamijala<sup>\*,‡,†,¶</sup>

<sup>†</sup>*Center for Atomistic Modelling and Materials Design, Indian Institute of Technology Madras, Chennai, 600036, India*

<sup>‡</sup>*Department of Chemistry, Indian Institute of Technology Madras, Chennai, 600036, India*

<sup>¶</sup>*Center for Molecular Materials and Functions, Indian Institute of Technology Madras, Chennai, 600036, India*

E-mail: [yamijala@smail.iitm.ac.in](mailto:yamijala@smail.iitm.ac.in)

## Abstract

Per- and poly-fluoroalkyl substances (PFAS) are a group of forever synthetic chemicals. They are widely utilized in industries and household appliances because of their remarkable stability and distinctive oil- and water-repellent properties. Despite their broad applications, unfortunately, PFAS are hazardous to all forms of life, including humans. In recent years, the environmental persistence of PFAS has raised significant interest in degrading these substances. However, the strong C–F bonds in these chemicals pose several challenges to their degradation. Plasmons of noble metal nanoparticles (NPs) offer many exciting applications, including photocatalytic reactions. However, an atomistic understanding of plasmon-driven processes remains elusive. In this work, using the real-time time-dependent density functional theory, we have studied the real-time formation of plasmons, hot-carrier generation, and subsequent direct hot-carrier transfer from metal NP to the PFAS. Our simulations show that there is an apparent direct hot-electron transfer from NP to PFAS. Moreover, using Ehrenfest dynamics simulations, we demonstrated that the transferred hot-electrons can efficiently degrade PFAS without requiring any external thermal bath. Thus, our work provides an atomistic picture of plasmon-induced direct hot-carrier transfer from NP to PFAS and the efficient degradation of PFAS. We strongly believe that this work generates the impetus to utilize plasmonic NPs to mitigate PFAS.

Per- and polyfluoroalkyl substances (PFAS) are man-made chemicals containing strong carbon-fluorine bonds.<sup>1–4</sup> Due to their unique properties, they have been widely used in various industries, such as aviation, food packaging, and textiles.<sup>5,6</sup> However, it was later realized that PFAS pose severe health challenges to various organisms, including humans.<sup>7</sup> Human beings are primarily exposed to PFAS through contaminated water and food.<sup>8–12</sup> Fur-

thermore, several recent studies have shown that PFAS can transfer from mother to child at the embryonic stage itself.<sup>13–15</sup> Considering the toxicological impacts of PFAS, several environmental agencies have banned a variety of these chemicals and released health advisories on their permissible daily intake limits. For example, the United States Environmental Protection Agency has specified 0.004 and 0.02 ng/L as the daily intake limit for perfluo-

rooctanoic acid (PFOA) and perfluorooctane-sulfonic acid (PFOS), respectively.<sup>16</sup> Given the harmful effects of PFAS, developing efficient technologies and strategies to eliminate these toxic substances from the environment is essential. Consequently, there has been a surge in global research to find effective methods to treat "PFAS-contaminated" water.<sup>17</sup> Numerous studies have explored both chemical and physical approaches to remediate PFAS.<sup>18–33</sup> However, existing treatment techniques such as ion-exchange, adsorption, and coagulation are ineffective in degrading these substances and often require further processing.

Recently, plasmon-induced processes have garnered significant attention for their ability to drive complex chemical reactions at the nanoparticle-molecule interface, such as water splitting,<sup>34–38</sup> H<sub>2</sub> dissociation,<sup>39–44</sup> CO<sub>2</sub> reduction,<sup>45–49</sup> and N<sub>2</sub> dissociation.<sup>50–53</sup> Plasmon-driven chemical reactions are induced through localized surface plasmon resonance (LSPR),<sup>54</sup> which refers to the collective excitation of free charge carriers in a metallic nanoparticle (NP) by absorbing visible light at the plasmon resonance frequency. In general, the plasmonic excitation decays to generate hot-carriers<sup>55</sup> (non-thermal carriers with excess energy), which can be transferred to nearby acceptors (molecules or semiconductors) to drive chemical reactions.<sup>56,57</sup> The transfer of hot-carriers to the molecule can occur either via indirect or direct charge transfer (CT) mechanisms.<sup>47,58,59</sup> In the indirect CT mechanism,<sup>60</sup> the plasmon decays within the NP to generate hot-carriers, which will be subsequently transferred to the molecule. In contrast, the direct CT mechanism<sup>61,62</sup> involves the decay of plasmons by directly exciting the electrons/holes from the NP into the unoccupied/occupied orbitals of the molecule. The difference between the direct and indirect processes depends on the interaction between the NP and adsorbate, where a van der Waals interaction promotes the indirect CT, whereas a chemical interaction is required to drive direct CT. Apart from these CT processes, the adsorbate could also undergo chemical transformation due to the field enhance-

ment or heat produced due to the plasmon decay within the NP.<sup>63–66</sup> Given the diverse range of processes that plasmonic excitations can trigger, there is a significant potential to utilize them for the degradation of PFAS. In this study, we explored the plasmon-induced CT dynamics at various NP-PFAS interfaces.

Between the direct and indirect CT processes, the indirect CT process<sup>47,59,67–69</sup> is generally less efficient in driving the chemical reactions since the generated hot-carriers experience energy losses due to scattering with other electrons and phonons within the NP before reaching the molecule.<sup>47,59,69–73</sup> At the same time, the direct CT process is generally found to be less probable than the indirect CT process, specifically at the NP-molecule interfaces.<sup>71,73</sup> Therefore, there is an apparent need to understand these processes at the atomic scale to further enhance the CT efficiencies from the NP to the molecule. However, unfortunately, disentangling the contributions of direct and indirect pathways is experimentally quite challenging because both these processes often occur simultaneously and at ultrafast time scale (< 100 fs). Computational studies using the real-time time-dependent density functional theory (RT-TDDFT) have been resourceful in obtaining atomic-scale insights into the plasmon-driven hot-carrier dynamics,<sup>55,74</sup> particularly in understanding the direct transfer of hot-carriers at the NP-molecule interfaces.

In this article, by considering Ag<sub>147</sub> as a prototypical example of a plasmonic NP and PFOA as a representative PFAS, we explored plasmon-driven hot-carrier dynamics across the NP-PFAS interface using RT-TDDFT. We present the temporal, spatial, and energetic pictures of the plasmon formation and hot-carrier generation at various interfacial geometries. Our study reveals that the dominant pathway for the plasmon decay occurs via the generation of hot-carriers within the NP, and the next dominant pathway includes the direct hot-electron transfer from the NP to PFOA. In contrast, the contributions to the plasmon decay from (i) direct hot-hole transfer from the

NP to PFOA and (ii) intramolecular excitations within PFOA are quite insignificant. Among the dominant pathways, since the direct CT pathway is efficient in driving chemical reactions, we explored this pathway in this work. To further tune the amount of direct CT, we studied various NP-molecule interfaces and considered different electric field polarization directions. We find that the maximum direct hot-electron transfer occurs when the molecule is kept along the  $z$ -direction of the nanoparticle and when the electric field is transversely polarized. Next, since higher electric field intensities are often used to dissociate molecules, we varied the pulse intensities from  $0.514 \text{ mV}/\text{\AA}$  to  $514 \text{ mV}/\text{\AA}$  and found that increasing pulse intensity results in a significant increase in the hot-electron transfer from the NP to PFOA.

Finally, to provide direct evidence for the plasmon-induced degradation of PFAS, we conducted Ehrenfest molecular dynamics (EMD) simulations on  $\text{Ag}_{55}\text{-PFOA}$  complex (due to the requirement of large computational resources, we could not conduct EMD simulations on  $\text{Ag}_{147}\text{-PFOA}$  complex). These EMD simulations clearly demonstrate that a PFOA molecules undergoes a near-complete degradation due to hot-electron transfer. We hope that this work provides the necessary impetus to leverage the potential of plasmonic technologies to degrade the forever and harmful PFAS.

**Plasmon formation and hot-carrier dynamics in NP-PFOA interface.** Figures 1(a) and 1(b) depict the optimized geometry and the projected density of states (pDOS) of the NP-PFOA interface. Clearly, the contributions to the total DOS of the NP-PFOA complex are mainly arising due to the NP, indicating that the adsorption of PFOA did not modify the electronic structure of the NP significantly. Figure 1(c) depicts the photoabsorption spectra of the bare NP, PFOA, and the NP-PFOA complex. The energy corresponding to the maximum absorption is at 3.83 eV for both NP and NP-PFOA complex, which corresponds to the plasmon resonance frequency (established later). Although there is a slight increment in the absorption intensity, the peak positions of the NP are mostly unaltered in the

presence of PFOA, indicating that the absorption spectrum of the complex has a major contribution from the NP. Also, the excitations in bare PFOA molecule (first peak is at 7.85 eV) are far away from the plasmonic peak of the NP, and their absorption intensity is quite small.

To establish the plasmonic nature of the 3.83 eV peak, we plotted the induced charge density of the complex (at 3.83 eV) in Figure 1(d), where orange and blue colors represent the accumulation and depletion of the electron density, respectively. The clear separation of the positive and negative charges at the opposite ends of the NP confirms the presence of LSPR. To further understand the nature of this excitation, we employed the Kohn-Sham (KS) decomposition technique (where each excitation is decomposed into individual KS electron-hole transitions) as a transition contribution map (TCM) in Figure 1(e).<sup>74</sup> In TCM, the red features correspond to strong positive constructive contributions from the KS transitions, the blue features correspond to large negative contributions that screen the plasmonic excitation, and the solid black diagonal line represents the resonant transitions at  $\omega_0 = 3.83 \text{ eV}$ . The nature of these transitions can be understood using the pDOS plots, which are given in Figures 1(e) and 1(f). The states near the Fermi level have major contributions from the s and p-states of the NP, whereas the d-states of the NP contribute majorly below  $-4 \text{ eV}$ . From these plots, it is evident that the bright red features in the TCM plot at around  $-1 \text{ eV}$  are arising due to the intraband sp-sp transitions, and the blue features at around  $-4 \text{ eV}$  are arising due to the interband d-sp transitions. The presence of several red features (sp-sp transitions) below the diagonal line establishes the plasmonic nature of the 3.83 eV excitation.<sup>55,74</sup> Together, these results demonstrate that exciting the system at 3.83 eV induces a plasmonic resonance in the NP-PFOA complex. Therefore, to probe the dynamics of plasmon formation and decay, we applied a Gaussian pulse (Eq. 1) that is tuned to the plasmonic peak. Since the plasmon formation and decay often occur in an ultrafast manner ( $\sim 1 - 30 \text{ fs}$ ),<sup>55,73,75</sup> we conducted the RT-TDDFT simulations for a duration of 30 fem-

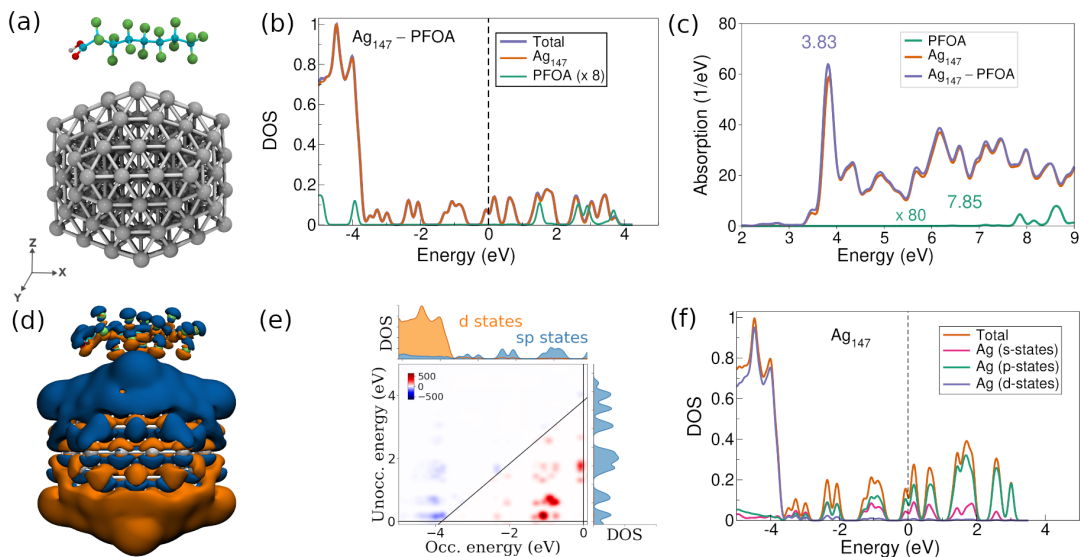


Figure 1: (a) Optimized geometry, and (b) Total and projected density of states (DOS) of NP-PFOA complex. (c) Photoabsorption spectra of PFOA (green), NP (orange), and NP-PFOA complex (purple) in the presence of a z-polarized light. For visualization purposes, the spectrum of PFOA is multiplied by a constant factor (80). (d) Induced charge density (with an isovalue of  $10^{-6}$  a.u.) in the complex at 3.83 eV. Orange and blue colors represent the accumulation and depletion of electrons, respectively. (e) Transition contribution map (TCM) of the complex at 3.83 eV. The solid diagonal line represents the resonant transitions at  $\omega_0 = 3.83$  eV. The red and blue features correspond to the strong positive and negative contributions from the KS transitions to the plasmonic excitation. PDOS of the d and sp-states of the NP are also shown. (f) Total and orbital projected DOS in the NP.

toseconds (fs). Also, this time period is found to be sufficient to capture the hot-carrier dynamics in the NP-PFAS complex.

Figure 2 (a) depicts the incident Gaussian pulse, which is centered at 10 fs and has a mild pulse strength of 514  $\mu\text{V}/\text{\AA}$ . The temporal changes in the induced dipole moment of the complex, due to its interaction with the pulse, are shown in Figure 2 (b). During the first 10 fs, the dipole moment of the complex oscillates in phase with the pulse and its magnitude increases with the pulse strength. However, while the pulse begins to decay after 10 fs, the dipole moment continues to increase, reaching its peak between 10-12 fs. Moreover, the induced dipole moment persists in the system until 27 fs, which is well-beyond the complete decay of the pulse at 15 fs. To further understand the relation between the dipole moment changes and the plasmon dynamics, we plotted the induced charge densities at five different instances of time, as shown in Figure 2(c), and these time instances are marked as vertical dashed lines in panel (b), labeled as (1)–(5). At 10.2 fs (1), after the pulse crossed its highest value, the dipole moment is significant due to the LSPR, as revealed by the induced density. Similarly, at 11 fs (2), the dipole moment is zero due to the vanishing surface-to-surface induced charge density oscillation. At 11.84 fs (3), the dipole moment is significant and switches its sign due to the polarity change in the induced charge density. At 20 fs (4), which is 5 fs after the complete decay of the pulse, the dipole moment has reduced significantly due to the dephasing of the plasmonic excitation as indicated by the lowered induced density. Finally, by 26.6 fs (5), the induced density becomes vanishingly small, indicating the lack of any collective excitations in the system, which explains the total decay in the dipole moment. Thus, the time-dependent dipole moment and the induced charge density provide an illustrative picture of plasmon formation and dephasing.

Next, to get an energetic picture of plasmon formation and hot-carrier generation, we employ the energy decomposition technique developed by Rossi *et al.*,<sup>55</sup> where the total energy stored in the excitation is primarily divided into

resonant and nonresonant transitions. Here, the nature of a transition is obtained by examining the difference between the KS transition energy ( $\omega_{ia} = \epsilon_a - \epsilon_i$ ) and the plasmon resonance energy ( $\omega_0$ ). When  $|\omega_{ia} - \omega_0| \geq 2\sigma$ , where  $\sigma$  is the pulse width ( $\sigma = \sqrt{2}/\tau_0$ , where  $\tau_0$  is the pulse width in time-space), the transitions are considered as the nonresonant transitions. In contrast, resonant transitions occur when  $|\omega_{ia} - \omega_0| \leq 2\sigma$ . Among the nonresonant transitions, the low-energy transitions ( $\omega_{ia} \leq \omega_0 - 2\sigma$ ) forms a plasmon, and the high-energy transitions ( $\omega_{ia} \geq \omega_0 + 2\sigma$ ) leads to plasmon dephasing. Specific to the noble metals, the coupled intraband sp-sp transitions are responsible for the formation of a plasmon, and the interband d-s transitions are responsible for the plasmon dephasing (as discussed earlier while explaining the TCM plots).

The time-dependent variation of the resonant and nonresonant transition contributions to the total energy stored in the excited state are depicted in Figure 2 (d). Before 10.2 fs, the total excited state energy has a major contribution only from the nonresonant transitions. This is because the incident light pulse is tuned to the LSPR frequency of the NP-PFOA complex, allowing the complex to absorb the energy from light and stay in an excited state. However, beyond 10.2 fs, the contribution from the resonant transitions increases since the plasmon begins to decay into hot-carriers (resonant transitions). At around 26.6 fs, the total energy is exclusively stored as the resonant contributions, indicating the complete decay of plasmons into hot-carriers. In addition to the resonant and nonresonant contributions, Figure 2 (d) also shows the portion of the total excited state energy that is stored in the form of Coulomb energy. Clearly, similar to the dipole moment, the Coulomb energy also oscillates with time, which is due to the strong oscillations in the surface charge density (Figure 2 (c)). Finally, it is important to note that our simulations show that the total excited state energy remains constant even after the pulse has ended (beyond 15 fs). However, in reality, the excited state energy will be dissipated to the environment through various processes, including radiative and nonradia-

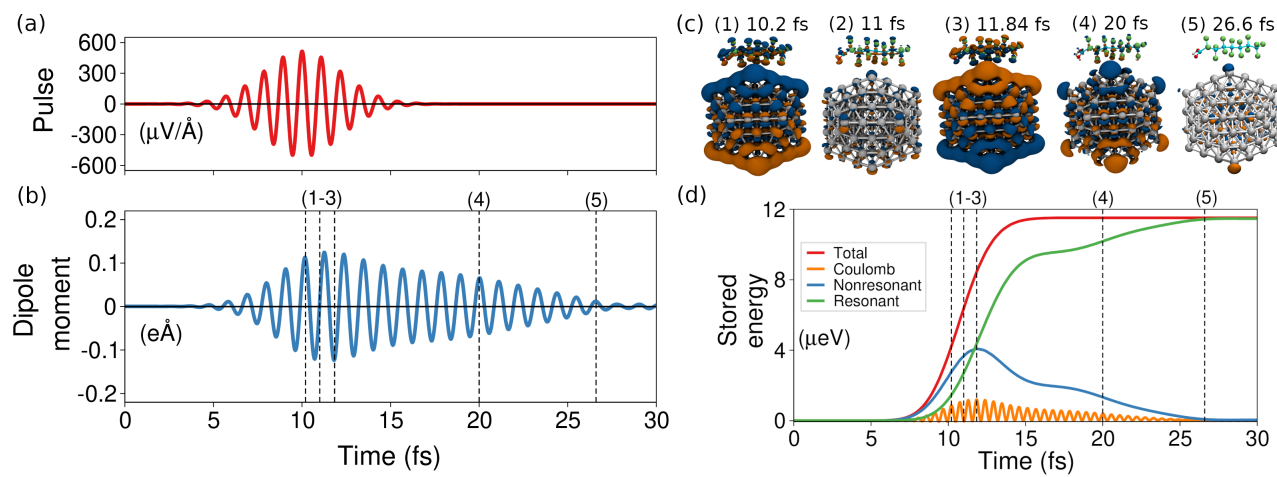


Figure 2: Real-time dynamics of a localized surface plasmon in  $\text{Ag}_{147}\text{-PFOA}$  at 3.83 eV. (a) Incident pulse, (b) induced dipole-moment, (c) induced charge density, and (d) energy stored in the excited state. Total energy (red) is divided into the nonresonant (blue) and resonant (green) contributions. Total energy in the form of Coulomb energy is also shown (orange). Vertical black dashed lines in panels (b) and (d) correspond to five different time instances: (1) 10.2, (2) 11, (3) 11.84, (4) 20, and (5) 26.6 fs.

tive decay channels,<sup>76,77</sup> in the order of several hundred picoseconds to nanoseconds. Studying these processes is beyond the scope of this article.

To further understand the distribution of total energy in terms of the individual KS electron-hole transitions, we plotted TCMs at 11 and 26.6 fs in Figure 3 (a). Here, the solid vertical and horizontal lines (white) correspond to the Fermi level, whereas the solid diagonal line is the resonance energy ( $\omega_0 = 3.83$  eV). The dashed diagonal lines that are drawn above and below the main diagonal line correspond to  $\omega_0 + 2\sigma$  and  $\omega_0 - 2\sigma$ , respectively. The TCM plot at 11 fs has several strong features both across the diagonal line and well below the diagonal line, indicating that the excited state energy is distributed among several KS transitions. Specifically, the features far below the resonance line (at  $\sim -1$  eV) contribute to the plasmonic (nonresonant) excitations arising due to the intraband sp-sp transitions. On the other hand, the interband d-s transitions are across the diagonal line, and they contribute to the single-particle (resonant) excitations. Therefore, at 11 fs, the total energy is distributed among both the resonant and nonresonant transitions. In contrast, the TCM plot at 26.6 fs has strong features only across the diagonal line,

suggesting that the entire energy at this time step is majorly stored in the resonant transitions.

Next, we studied the energetic spread of the resonant and nonresonant carriers across the Fermi level by using the transition probability,<sup>55</sup>  $P_{ia}(t) = |\delta\rho_{ia}(t)/\sqrt{f_i - f_a}|^2$ , where  $f_i$  and  $f_a$  are the ground-state occupations in the basis of the occupied ( $i$ ) and unoccupied ( $a$ ) KS states, respectively, and the KS transition density matrix is defined as  $\delta\rho_{ia}(t) = \rho_{ia}(t) - \rho_{ia}(0)$ . The occupations of electrons in state  $a$  and holes in state  $i$  are given by  $P_a^e(t) = \sum_i P_{ia}(t)$  and  $P_i^h(t) = \sum_a P_{ia}(t)$ , respectively. The hot-electron occupation probability across various KS eigenstates at time  $t$  (or simply, the hot-electron distribution) can be computed as  $P_e(E, t) = \sum_a P_a^e(t)G_a(E)$ . Similarly, the hot-hole distribution is calculated as  $P_h(E, t) = \sum_i P_i^h(t)G_i(E)$ . Here,  $G_a(E)$  and  $G_i(E)$  are Gaussian broadening functions. The occupation probabilities of the KS states for both holes and electrons that are arising due to both the resonant and nonresonant transitions are shown in Figure 3 (b) at 11 and 26.6 fs. At 11 fs, clearly the nonresonant contributions are the dominant ones, and the corresponding carriers are majorly distributed between -1 to 1 eV across the Fermi level. There are also a few car-

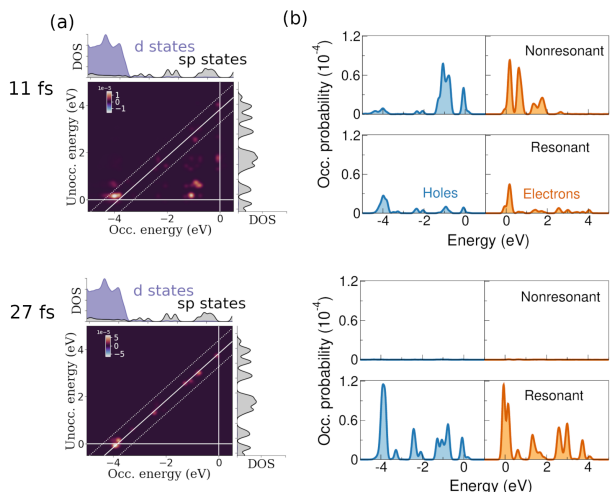
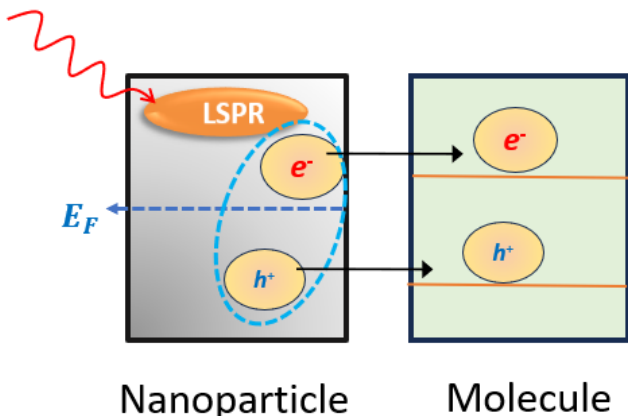


Figure 3: (a) Total energy represented as a TCM at 11 and 26.6 fs, where the solid vertical and horizontal white lines represent the Fermi level, and the solid diagonal line represents the plasmon resonance energy ( $\omega_0$ ). The white dashed lines are drawn at  $\omega_0 - 2\sigma$  and  $\omega_0 + 2\sigma$ , respectively, where  $\sigma$  is the pulse width. (b) Occupation probabilities of KS states across the Fermi-level for both holes (blue) and electrons (orange). The upper and lower panels in each sub-figure represent the nonresonant and resonant transitions, respectively.

riers due to the resonant transitions, which are primarily localized at -4 eV for the holes and closer to the Fermi level for the electrons. In other words, the generation of hot-holes started at 11 fs itself (due to the interband transitions). In contrast, at 26.6 fs, the KS states are primarily occupied by the carriers arising due to the resonant transitions, with negligible contributions from the nonresonant transitions. It is apparent that the carriers at 26.6 fs have energies that are far away from the Fermi level, indicating that these are hot-carriers. Interestingly, the majority of the hot-electrons lie near the Fermi level, arising from the plasmon dephasing due to the interband d-sp transitions as their energy is in resonance with the plasmon excitation energy of  $\omega_0$ . Notably, the hot-electrons also have a significant distribution near 3 eV of energy and a few electrons also up to the plasmon resonance energy  $\omega_0$ . So far, we clearly established (i) the temporal evolution of the plasmon formation and decay, (ii) the energetic distribution of hot-carriers, and (iii) the hot-carrier dynamics. Next, we will describe the plasmon-induced hot-carrier transfer from the NP to the PFOA molecule.

**Plasmon-induced hot-carrier transfer.** As discussed in the introduction, the hot-carriers generated during the plasmon decay can be transferred to the PFOA molecule primarily via two pathways, namely, the indirect and direct charge transfer mechanisms. A schematic of these pathways is shown in Figure 4. The direct charge transfer mechanism can further be divided into (i) direct hot-electron transfer (DHET) and (ii) direct hot-hole transfer (DHHT). In DHET (DHHT), the electrons in the occupied states of the NP (molecule) transfer to the unoccupied states of the molecule (NP), creating electrons (holes) in the molecule and holes (electrons) in the NP. To compute the plasmon-induced direct charge transfer processes, we followed the method proposed by Kumar *et al.*<sup>61,78</sup> Here, we partitioned the simulation box into two spatial regions separating the NP and PFOA and computed the hot-carrier transfer by considering the transitions among the occupied and unoccupied orbitals of these two components. Naturally,

(a) Indirect charge transfer



(b) Direct charge transfer

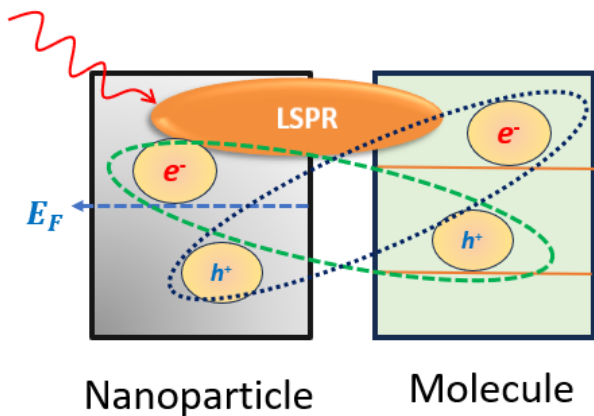


Figure 4: A schematic representation of plasmon-induced charge transfer dynamics from NP to molecule. (a) and (b) correspond to the indirect and direct charge transfer processes, respectively. A laser pulse tuned to the plasmon resonance energy is shown in red color. In the indirect process, LSPR decays within the NP by creating the hot-electron and hole pairs, which then transfer to the nearby molecule. In contrast, in the direct charge transfer process, LSPR decays by directly generating the hot-carriers in the molecule.

four kinds of transitions are feasible, namely, NP  $\rightarrow$  NP, PFOA  $\rightarrow$  PFOA, NP  $\rightarrow$  PFOA, and PFOA  $\rightarrow$  NP, where the last two transitions correspond to the DHET and DHHT processes, respectively. The calculated number of carriers generated via four partial processes is shown in Figure 5 (a). Among the four kinds of transitions, the plasmon decay predominantly occurs through the creation of hot-carriers within the NP (with a probability of around 93 %). The next dominant mechanism is the DHET, which occurs with a probability of 6.8 %. As mentioned in the introduction, it should be noted that the direct charge transfer process is less probable than the indirect charge transfer process, specifically in NP-molecule complexes.<sup>73,78,79</sup> For example, earlier works have reported the DHET with a probability of  $\sim 0.8\%$  for the Au<sub>87</sub>-CO complex<sup>79</sup> and  $\sim 2\%$  for Ag<sub>147</sub>-CO complex.<sup>78</sup> Compared to these studies, the observed 7% DHET is significantly higher. Moreover, as shown in our Ehrenfest simulations (presented later), this percentage is large enough to drive the degradation of PFAS. The probabilities for the other two processes, namely, the DHHT

and intramolecular excitations, are insignificant. Interestingly, the plasmon decay into the hot-carriers saturates beyond 27 fs, and justifies our simulation duration (30 fs). In Figure 5 (a), the number of carriers generated through each process is obtained by summing the weighted transition probabilities. For example, the number of carriers involved in the DHET process are computed as:  $P_e^{\text{NP} \rightarrow \text{PFOA}}(t) = \sum_{ia} P_{ia}^{\text{NP} \rightarrow \text{PFOA}}(t) = \sum_{ia} w_i^{\text{NP}} w_a^{\text{PFOA}} P_{ia}(t)$ , where the weight/contribution of an  $n^{\text{th}}$  KS state towards each subsystem is computed as  $w_n^{\text{NP}} = \int_{\mathbf{r} \in \text{NP}} |\psi_n(\mathbf{r})|^2 d\mathbf{r}$  and  $w_n^{\text{PFOA}} = \int_{\mathbf{r} \in \text{PFOA}} |\psi_n(\mathbf{r})|^2 d\mathbf{r}$ , with the constraint  $w_n^{\text{NP}} + w_n^{\text{PFOA}} = 1$ .

The weighted transition probabilities can also be used to obtain the energetic distribution of hot-carriers across the Fermi level. For example, the energetic distribution of hot-carriers generated through the DHET mechanism is given by  $P_e^{\text{NP} \rightarrow \text{PFOA}}(E, t) = \sum_{ia} P_{ia}^{\text{NP} \rightarrow \text{PFOA}}(t) G_a(E)$ , where  $G_a(E)$  is the Gaussian broadening. This distribution, computed at 27 fs, is shown in the upper panel of Figure 5 (b). Here, the blue and orange shaded

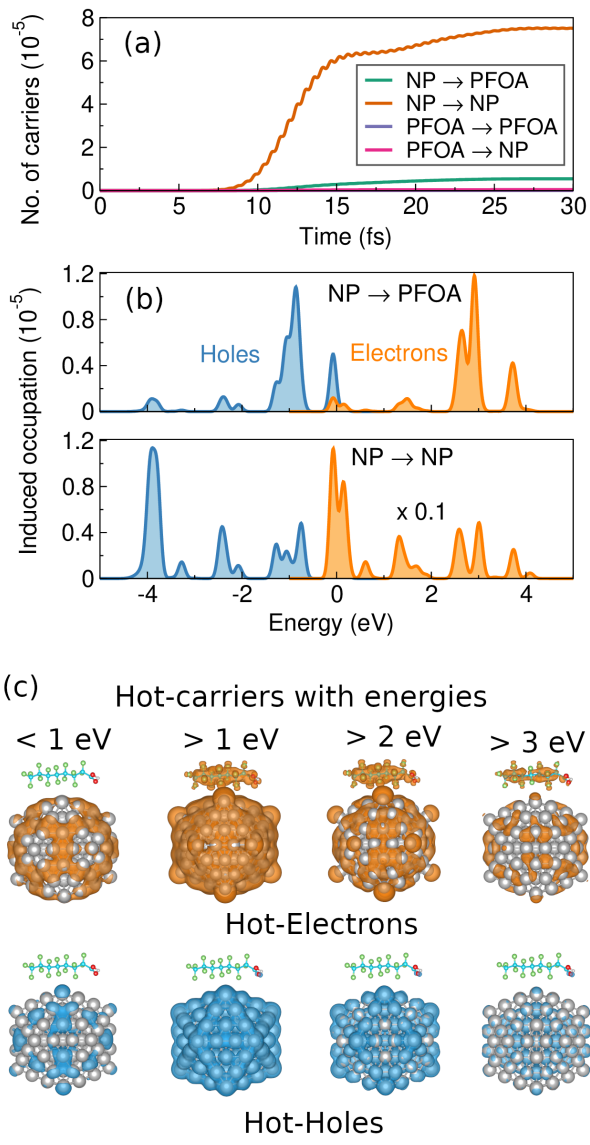


Figure 5: (a) The number of carriers generated via the four partial processes, namely, the DHET (green), excitations within the NP (orange curve), intramolecular excitations (purple), and the DHHT (pink curve). (b) Energetic distribution of the hot-carriers relative to the Fermi energy for the DHET and the intra-NP excitation processes. The distribution is computed at 27 fs (by this time the plasmon is completely decayed into hot-carriers). (c) The spatial distribution of hot-electrons and holes at various energies.

curves represent the hot-hole and hot-electron distributions, respectively. Clearly, the majority of the hot-electrons generated through the DHET mechanism have energies around 3 eV (i.e., they are highly energetic), and a few of them have even energies close to the plasmon resonance energy (3.83 eV). In contrast, the majority of the hot-holes generated through the DHET mechanism are within 1 eV from the Fermi level. Similarly, among the hot-carriers generated due to the NP  $\rightarrow$  NP transitions (lower panel of Figure 5 (b)), the majority of the hot-electrons have energies closer to the Fermi energy and hot-holes have energies of about  $-4$  eV.

Since the energetic distribution of hot-carriers plays a crucial role in the hot-carrier-mediated chemical reactions, it is essential to understand the observed differences in the hot-electron and hot-hole distributions. One of the primary factors that strongly influences these distributions is the electronic structure of the complex. Moreover, since the DHET mechanism involves the transition of electrons from the occupied orbitals of NP to the unoccupied orbitals of PFOA, a careful examination of the positions of occupied orbitals of NP and unoccupied orbitals of PFOA (that align with the plasmon resonance energy 3.83 eV) will help us to comprehend the hot-carrier distribution. To this end, we carefully examined the PDOS of the NP-PFOA complex (Figure 1b). From the figure, it is evident that the unoccupied states of the PFOA have larger densities between  $\sim 1.25$ - $1.75$  eV and  $\sim 2.5$ - $3.5$  eV. For the incident laser pulse to create resonant transitions into these unoccupied states, the corresponding occupied orbitals of the NP must be located in the energy ranges between  $-2.75$  to  $-2.25$  and  $-1.5$  to  $-0.5$  eV, respectively. Otherwise, the condition for resonance will not be satisfied. Between these two ranges, a larger number of NP density of states are continuously available between  $-1.5$  to  $-0.5$  eV. Moreover, molecular orbital plots (Figure S1) reveal the presence of several hybridized NP and PFOA states in this range, which play a crucial role in plasmon dephasing through the direct charge transfer pathway. Therefore, there is a greater probability for the

electrons of NP with energies in the range of -1.5 to -0.5 eV to be transferred to the unoccupied orbitals of PFOA in the range of  $\sim$ 2.5-3.5 eV, generating hot-holes in  $\sim$ 1 eV range and hot-electrons in  $\sim$ 3 eV range, respectively, which is in agreement with the hot-carrier distribution depicted in the upper panel of Figure 5(b). A similar analysis will explain the hot-electron transfer to PFOA at other energies and also the hot-carrier distribution due to the NP  $\rightarrow$  NP and DHHT transitions (for explanation, see section A of the supplementary information).

Next, we provided the spatial distribution of these excess-energy electrons and holes in Figure 5(c). Specifically, we presented the distribution of carriers whose energies are (i) within 1 eV, (ii)  $>$  1 eV, (iii)  $>$  2 eV, and (iv)  $>$  3 eV with respect to the Fermi level. The corresponding equations that we used to obtain these spatial distribution plots are provided in section B of the supplementary information. As depicted in these figures, the electrons with energies between 0 to 1 eV are mostly localized on the NP. In contrast, electrons with energies larger than 1 eV (hot-electrons) are delocalized over the entire NP-PFOA complex. Notably, some of the highly energetic electrons (with energies greater than 2 and 3 eV) are present all over the PFOA molecule. *This result not only establishes the electron transfer from the NP to the PFOA but also unambiguously demonstrates the transfer of highly energetic hot-carriers (with energies  $>$  3 eV) to PFOA, which can readily dissociate the strong C–F bonds of the PFOA molecule.* Importantly, several earlier ab initio molecular dynamics simulations have demonstrated that PFAS molecules decompose in an ultrafast manner in the presence of excess electrons.<sup>80–83</sup> Since plasmon decay transfers excess-energy hot-electrons to PFAS, they will be much more efficient at degrading PFAS compared to regular excess electrons. It should also be noted that since the hot-electrons can have energies only up to the plasmon resonance energy  $\omega_0$ , we did not observe any electrons with energy greater than 4 eV. Unlike hot-electrons, at all energies, hot-holes are predominantly localized over the NP (except for a minute fraction

that can be seen near the oxygen atoms in the PFOA molecule). Thus, our results indicate that, in the absence of other external factors, hot-electron transfer is the primary mechanism through which a PFOA molecule will be degraded in the presence of a plasmonic NP.

Next, we analyzed the effects of field strength and orientation of the PFOA molecule relative to the NP. As shown in Figure 6, the hot-electron transfer from NP to PFOA increases significantly at higher pulse intensities. Specifically, we observed several orders of magnitude increment in the electron transfer by increasing the field strength from 0.514 mV/Å to 514 mV/Å. Moreover, the occupation probabilities at different time scales clearly establish the fact that the plasmon-dephasing before 11 fs is majorly occurring due to the NP  $\rightarrow$  NP transitions, whereas the dephasing at later timescales is also influenced by the NP  $\rightarrow$  PFOA (DHET) transitions. At the same time, the increase in intensity does not have any effect on the energy of the generated hot-electrons. Overall, we find that increasing intensity facilitates a larger amount of hot-electron transfer from NP to PFOA, further promoting the efficient degradation of the PFOA molecule.

For investigating the effects of PFOA orientation relative to the NP on the DHET mechanism, we considered two more orientations (apart from the orientation that we considered in Figure 1(a), which we will refer to as Interface-1.). We refer to the two new orientations as Interface-2 and Interface-3, respectively (see the insets in Figures 6(d) and 6(e)). In Interface-1, the carbon chain of the PFOA molecule is perpendicular to the diameter of the NP. In Interface-2, the carbon chain of the molecule is parallel to the diameter of the NP, with the oxygen atoms positioned near the nanoparticle. Interface-3 is similar to Interface-2, except that the oxygen atoms of the molecule are facing away from the NP (i.e., the PFOA molecule is rotated by 180° compared to Interface-2). The photoabsorption spectra of these interfaces for applied electric fields polarized along the x and z-directions are provided in Figures 6(d) and 6(e). No

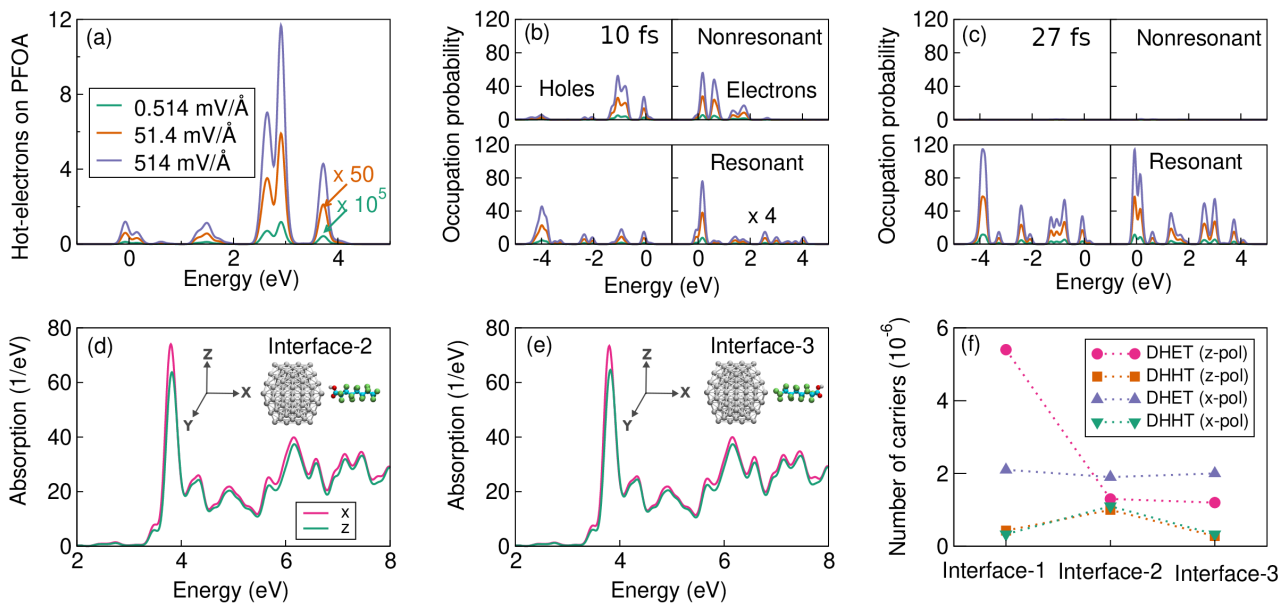


Figure 6: Pulse intensity and NP-PFOA interface-dependent results. (a) Energetic distribution of the number of hot-electrons transferred to PFOA through the direct transfer mechanism at various pulse intensities. Appropriate numbers, as marked, were used as multiplicative factors for visualization purposes. (b) and (c) Intensity-dependent occupation probability distribution of electrons and holes with respect to the Fermi energy for the resonant and nonresonant transitions at two different time instances (10 and 27 fs). (d) and (e) Photoabsorption spectra of two other interfaces (Interface-2 and Interface-3) for  $x$ - and  $z$ -polarized electric fields. The inset shows the interface structures. (f) Variation in the number of hot-carriers generated in the PFOA molecule through the direct transfer mechanism with a change in the interfacial geometry and laser polarization.

tably, the photoabsorption peaks of these interfaces remain unchanged with variations in PFOA orientation, indicating the minimal effect of PFOA on the absorption spectrum of the complex. Also, since the NP is isotropic, the electric field polarizations did not create any significant changes in the spectrum. The number of hot-carriers generated on the molecule via DHET and DHHT processes in all three interfaces and for both  $x$  and  $z$ -polarized electric fields is shown in Figure 6(f). The DHET is found to be highest in Interface-1 under the  $z$ -polarized electric field. In contrast, DHHT is polarization-independent and reaches its maximum in Interface-2.

### Plasmon-induced degradation of PFAS.

Due to the substantial computational cost associated with the Ehrenfest molecular dynamics (EMD) simulations, we considered a smaller NP ( $\text{Ag}_{55}$ ) for studying the degradation dynamics of PFOA. Currently, with GPAW, the EMD simulations can only be conducted in the finite-difference TDDFT (FD-TDDFT) method. Moreover, since this method is not compatible with the Gritsenko, van Leeuwen, van Lenthe, and Baerends solid correlation (GLLB-SC) functional, we used the PBE functional in all our EMD calculations. For consistency, we used the same method to compute the absorption spectrum of the  $\text{Ag}_{55}$ –PFOA complex. As shown in Figure S2, the  $\text{Ag}_{55}$ –PFOA complex exhibits a plasmonic peak at 3.6 eV, and the corresponding LSPR frequency is used in our EMD simulations. To observe the plasmon-induced molecular dissociation, earlier theoretical studies have used the field intensities in the order of  $10^{13} - 10^{15} \text{ W cm}^{-2}$  ( $1-10 \text{ V}/\text{\AA}$ ). Following these works, we considered a laser pulse (Eq. 1) with a field strength ( $\varepsilon_0$ ) of  $1.0 \text{ V}/\text{\AA}$  and conducted the EMD simulations.

Figure 7a depicts the variation in the C–F bond distances as a function of the simulation duration. Below 50 fs, the C–F bond distances were oscillating between  $\sim 1.25$  and  $\sim 1.75 \text{ \AA}$ , i.e., across the C–F equilibrium bond distance ( $\sim 1.37 \text{ \AA}$ ). After 50 fs, several of the C–F bond distances increased beyond  $2 \text{ \AA}$ , and some of them even reached values up to  $3.5 \text{ \AA}$ , providing direct evidence for the plasmon-

induced degradation of PFOA. Figure 7b shows the NP–PFOA geometries at three different time instances, namely, 0, 60, and 90 fs, where the near complete degradation of PFOA can be observed by 90 fs. Together, these results establish that the plasmon-induced DHET enables the degradation of PFAS.

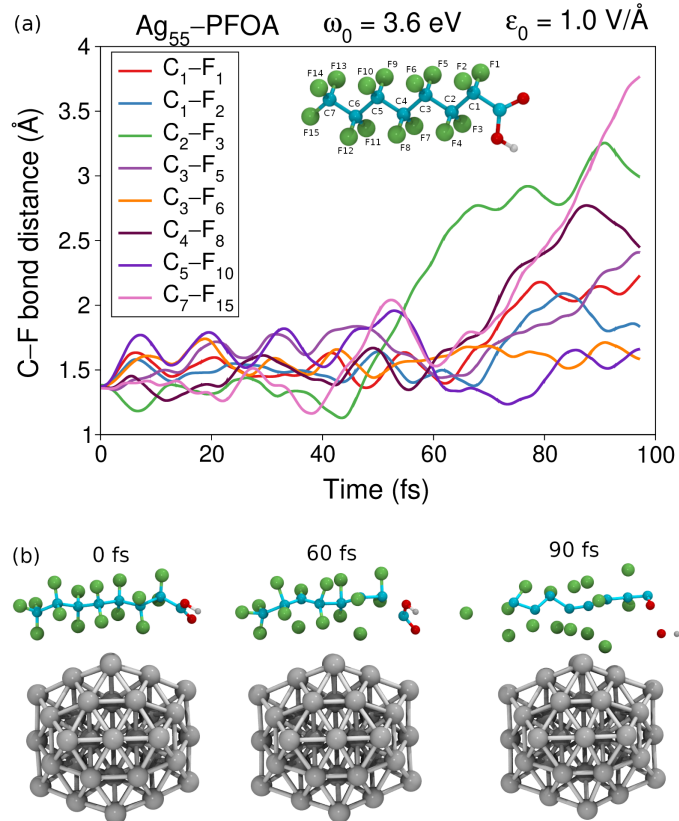


Figure 7: Plasmon-induced dissociation of a PFOA molecule in  $\text{Ag}_{55}$ –PFOA complex. (a) Variation in the C–F bond distances with time. The inset shows the PFOA molecule and the labeling scheme that we used to denote various C–F bonds in the molecule. The plasmonic peak energy and the field intensity are also provided. (b) The snapshots of the NP–PFOA complex at 0 fs, 60 fs, and 90 fs of the Ehrenfest molecular dynamics simulation. The near-complete degradation of the PFOA molecule can be seen at 90 fs.

**Conclusions.** We reported the real-time evidence of plasmon-induced direct hot-electron transfer from metal NPs to PFAS and provided an atomistic understanding of this novel degradation mechanism. Through RT-TDDFT simulations, we established that plasmonic exci-

tation in Ag<sub>147</sub>-PFOA complex occurs within 8–12 fs and decays into hot-carriers in an ultrafast (27 fs) manner through various decay channels. Specifically, we showed that the chemical interface damping facilitates the direct transfer of highly energetic hot-electrons (up to plasmon resonance energy  $\omega_0$ ) from NP to PFOA with  $\sim 7\%$  probability in Ag<sub>147</sub>-PFOA and with  $\sim 17\%$  probability in Ag<sub>55</sub>-PFOA. These hot-electrons delocalize over the entire PFOA molecule and enable the dissociation of its strong C-F bonds. Among various modifications, we find that laser intensity can significantly enhance the amount of direct hot-electron transfer. These findings provide atomistic insights into plasmon-induced hot-carrier dynamics in NP-PFAS complexes and establish a clear framework for leveraging plasmonic systems to degrade harmful water pollutants. By exploring different NP geometries, compositions, and adsorption sites, future studies can further optimize these plasmonic hot-carrier systems to drive advances in water treatment.

**Methods.** All the ground state optimization calculations were performed using density functional theory along with the Perdew–Burke–Ernzerhof (PBE) exchange-correlation functional,<sup>84</sup> as implemented in the GPAW code<sup>85,86</sup> in conjunction with the atomic simulation environment (ASE).<sup>87</sup> The Broyden–Fletcher–Goldfarb–Shanno (BFGS) optimizer<sup>88</sup> was used for the geometry optimization. All the systems were considered to be optimized when the maximum forces on each atom were less than 0.01 eV/Å. In the optimized NP-PFOA complex, the minimum distance between the NP and PFOA (between Ag and F atoms) was found to be around 3 Å. A minimum of 6 Å vacuum was used in all directions to minimize the interaction between their periodic images. A grid spacing of 0.2 Å and double-zeta polarized (DZP) basis sets were used.

The excited-state calculations were performed using the RT-TDDFT formalism. The projector augmented-wave method was utilized to represent the wave functions, employing a linear combination of atomic orbitals (LCAO).<sup>89</sup> To properly describe the d-states in Ag atoms,

the Gritsenko, van Leeuwen, van Lenthe, and Baerends solid correlation (GLLB-SC)<sup>90,91</sup> exchange-correlation functional was used in these calculations. All the dynamical responses were described using the random phase approximation (RPA). To reduce the computational cost while maintaining the numerical accuracy, a grid spacing of 0.3 Å was used in the time-dependent simulations. The photoabsorption spectra were obtained by considering a Delta-kick perturbation. The strength of the perturbation was kept small (0.514 mV/Å) to ensure that the system remained in the linear response regime. To obtain smooth photoabsorption spectra, a Gaussian broadening of 0.07 eV (with a full-width half maximum of 0.16 eV) was used while conducting the Fourier transform of the dipole moment.

Next, we used a monochromatic ultrafast Gaussian pulse of the form

$$\varepsilon(t) = \varepsilon_0 \cos(\omega_0(t - t_0)) e^{-(t-t_0)^2/\tau^2} \quad (1)$$

to excite the LSPR and to initiate the real-time dynamics of electrons in NP-PFOA. With a pulse duration of  $\tau_0 = 3$  fs, the pulse frequency  $\omega_0$  was tuned to the plasmon resonance. Moreover, the pulse is centered at  $t_0 = 10$  fs, and the pulse strength ( $\varepsilon_0 = 0.514$  mV/Å) was kept small to keep the system in the linear response regime. In all the real-time simulations, we used a time step of 10 attoseconds with a total simulation duration of 30 femtoseconds. The pulse convolution method implemented by Rossi *et al.*<sup>55</sup> was used to obtain the time-dependent density matrix, energy stored in the excited state, and the other hot-carrier analysis. EMD simulations were conducted with a monochromatic ultrafast Gaussian pulse of the form in Eq. 1 and with a pulse strength of 1 V/Å for 90 fs duration with a time step of 10 as. Various software packages, namely VMD,<sup>92</sup> VESTA,<sup>93</sup> NumPy,<sup>94</sup> and GRACE were used for visualization, data processing, and plotting.

**Acknowledgement** P.K.V. thanks the CAMMD group for financial support. S.K.N. acknowledges the Prime Minister's Research Fellowship from the government of India (PMRF ID: 2501800). K.B. acknowledges

the University Grants Commission (UGC) for the financial support. S.S.R.K.C.Y. acknowledges the financial support of IIT Madras through the MPHYSIS faculty fellowship and its new faculty support grants NFSG (IP2021/0972CY/NFSC008973), NFIG (RF2021/0577CY/NFIG008973), and DST-SERB (SRG/2021/001455). All the authors acknowledge National Supercomputing Mission (NSM), Government of India, for providing computing resources of ‘PARAM PORUL’.

## Supporting Information Available

The supporting information contains additional data on the theoretical explanation of the possibility of the direct and indirect charge transfer processes, energy levels of the Kohn-Sham orbitals, and the photoabsorption spectrum of NP-PFOA with smaller NP. It is available free of charge.

### Notes

The authors declare no competing financial interest.

## References

- (1) Fromme, H.; Tittlemier, S. A.; Völkel, W.; Wilhelm, M.; Twardella, D. Perfluorinated compounds – Exposure assessment for the general population in western countries. *Int. J. Hyg. Env. Health* **2009**, *212*, 239–270.
- (2) Buck, R. C.; Franklin, J.; Berger, U.; Conder, J. M.; Cousins, I. T.; de Voogt, P.; Jensen, A. A.; Kannan, K.; Mabury, S. A.; van Leeuwen, S. P. Perfluoroalkyl and polyfluoroalkyl substances in the environment: Terminology, classification, and origins. *Integ. Env. Ass. Management* **2011**, *7*, 513–541.
- (3) Çeçen, F.; Tezel, U. *Hazardous Pollutants in Biological Treatment Systems: Fundamentals and a Guide to Experimental Research*; IWA Publishing, 2017.
- (4) Glüge, J.; Scheringer, M.; Cousins, I.; Dewitt, J.; Goldenman, G.; Herzke, D.; Lohmann, R.; Ng, C.; Trier, X.; Wang, Z. An overview of the uses of per- And polyfluoroalkyl substances (PFAS). *Env. Sci. Proc. Impacts* **2020**, *22*, 2345–2373.
- (5) Kiss, E. *Fluorinated Surfactants and Repellents*; Marcel Dekker AG, 2001.
- (6) Uwayezu, J. N.; Carabante, I.; Lejon, T.; van Hees, P.; Karlsson, P.; Hollman, P.; Kumpiene, J. Electrochemical degradation of per- and poly-fluoroalkyl substances using boron-doped diamond electrodes. *J. Env. Management* **2021**, *290*, 112573.
- (7) Ao, J.; Yuan, T.; Xia, H.; Ma, Y.; Shen, Z.; Shi, R.; Tian, Y.; Zhang, J.; Ding, W.; Gao, L.; Zhao, X.; Yu, X. Characteristic and human exposure risk assessment of per- and polyfluoroalkyl substances: A study based on indoor dust and drinking water in China. *Env. Pollution* **2019**, *254*, 112873.
- (8) Roth, K.; Imran, Z.; Liu, W.; Petriello, M. C. Diet as an Exposure Source and Mediator of Per- and Polyfluoroalkyl Substance (PFAS) Toxicity. *Front. Toxicol.* **2020**, *2*, 601149.
- (9) Wee, S. Y.; Aris, A. Z. Revisiting the “forever chemicals”, PFOA and PFOS exposure in drinking water. *npj Clean Water* **2023**, *6*, 57.
- (10) Wee, S. Y.; Aris, A. Z. Environmental impacts, exposure pathways, and health effects of PFOA and PFOS. *Ecotoxicol. Env. Safety* **2023**, *267*, 115663.
- (11) Abunada, Z.; Alazaiza, M. Y. D.; Bashir, M. J. K. An Overview of Per- and Polyfluoroalkyl Substances (PFAS) in the Environment: Source, Fate, Risk and Regulations. *Water* **2020**, *12*, 3590.
- (12) Panieri, E.; Baralic, K.; Djukic-Cosic, D.; Buha Djordjevic, A.; Saso, L. PFAS

- Molecules: A Major Concern for the Human Health and the Environment. *Toxics* **2022**, *10*, 44.
- (13) Manzano-Salgado, C. B.; Casas, M.; Lopez-Espinosa, M.-J.; Ballester, F.; Basterrechea, M.; Grimalt, J. O.; Jiménez, A.-M.; Kraus, T.; Schettgen, T.; Sunyer, J.; Vrijheid, M. Transfer of perfluoroalkyl substances from mother to fetus in a Spanish birth cohort. *Env. Research* **2015**, *142*, 471–478.
- (14) Starling, A.; Adgate, J.; Hamman, R.; Kechris, K.; Calafat, A.; Ye, X.; Dabelea, D. Perfluoroalkyl Substances during Pregnancy and Offspring Weight and Adiposity at Birth: Examining Mediation by Maternal Fasting Glucose in the Healthy Start Study. *Env. Health Perspect.* **2017**, *125*, 067016.
- (15) Szilagyi, J.; Avula, V.; Fry, R. Perfluoroalkyl Substances (PFAS) and Their Effects on the Placenta, Pregnancy, and Child Development: a Potential Mechanistic Role for Placental Peroxisome Proliferator-Activated Receptors (PPARs). *Current Env. Health Reports* **2020**, *7*.
- (16) EPA, U. Drinking water health advisories for PFOA and PFOS. " **2016**,
- (17) Rahman, M. F.; Peldszus, S.; Anderson, W. B. Behaviour and fate of perfluoroalkyl and polyfluoroalkyl substances (PFASs) in drinking water treatment: A review. *Water Research* **2014**, *50*, 318–340.
- (18) Dixit, F.; Dutta, R.; Barbeau, B.; Berube, P.; Mohseni, M. PFAS removal by ion exchange resins: A review. *Chemosphere* **2021**, *272*, 129777.
- (19) Gagliano, E.; Sgroi, M.; Falciglia, P. P.; Vagliasindi, F. G.; Roccaro, P. Removal of poly- and perfluoroalkyl substances (PFAS) from water by adsorption: Role of PFAS chain length, effect of organic matter and challenges in adsorbent regeneration. *Water Research* **2020**, *171*, 115381.
- (20) Biplob Kumar Pramanik, S. K. P.; Suja, F. A comparative study of coagulation, granular- and powdered-activated carbon for the removal of perfluoroctane sulfonate and perfluorooctanoate in drinking water treatment. *Env. Technology* **2015**, *36*, 2610–2617.
- (21) Gar Alalm, M.; Boffito, D. C. Mechanisms and pathways of PFAS degradation by advanced oxidation and reduction processes: A critical review. *Chem. Eng. J.* **2022**, *450*, 138352.
- (22) Radjenovic, J.; Duinslaeger, N.; Avval, S. S.; Chaplin, B. P. Facing the Challenge of Poly- and Perfluoroalkyl Substances in Water: Is Electrochemical Oxidation the Answer? *Env. Sci. Technology* **2020**, *54*, 14815–14829.
- (23) Cui, J.; Gao, P.; Deng, Y. Destruction of Per- and Polyfluoroalkyl Substances (PFAS) with Advanced Reduction Processes (ARPs): A Critical Review. *Env. Sci. Technology* **2020**, *54*, 3752–3766.
- (24) Cao, H.; Zhang, W.; Wang, C.; Liang, Y. Sonochemical degradation of poly- and perfluoroalkyl substances – A review. *Ultrasonics Sonochem.* **2020**, *69*, 105245.
- (25) Leung, S. C. E.; Shukla, P.; Chen, D.; Eftekhari, E.; An, H.; Zare, F.; Ghasemi, N.; Zhang, D.; Nguyen, N.-T.; Li, Q. Emerging technologies for PFOS/PFOA degradation and removal: A review. *Sci. Total Env.* **2022**, *827*, 153669.
- (26) Hao, S.; Choi, Y. J.; Deeb, R. A.; Strathmann, T. J.; Higgins, C. P. Application of Hydrothermal Alkaline Treatment for Destruction of Per- and Polyfluoroalkyl Substances in Contaminated Groundwater and Soil. *Env. Sci. Technology* **2022**, *56*, 6647–6657.
- (27) Krause, M. J.; Thoma, E.; Sahle-Damesessie, E.; Crone, B.; Whitehill, A.;

- Shields, E.; Gullett, B. Supercritical Water Oxidation as an Innovative Technology for PFAS Destruction. *J. Env. Eng.* **2022**, *148*, 05021006.
- (28) Song, Z.; Tang, H.; Wang, N.; Zhu, L. Reductive defluorination of perfluorooctanoic acid by hydrated electrons in a sulfite-mediated UV photochemical system. *J. Hazard. Mater.* **2013**, *262*, 332–338.
- (29) Yamijala, S. S.; Shinde, R.; Hanasaki, K.; Ali, Z. A.; Wong, B. M. Photo-induced degradation of PFASs: Excited-state mechanisms from real-time time-dependent density functional theory. *J. Hazard. Mater.* **2022**, *423*, 127026.
- (30) Ali, Z. A.; Yamijala, S. S.; Wong, B. M. A review of emerging photoinduced degradation methods for per- and polyfluoroalkyl substances in water. *Current Opini. Chem. Eng.* **2023**, *41*, 100947.
- (31) Xin, X.; Kim, J.; Ashley, D. C.; Huang, C.-H. Degradation and Defluorination of Per- and Polyfluoroalkyl Substances by Direct Photolysis at 222 nm. *ACS EST Water* **2023**, *3*, 2776–2785.
- (32) Raza, A.; Bardhan, S.; Xu, L.; Yamijala, S. S. R. K. C.; Lian, C.; Kwon, H.; Wong, B. M. A Machine Learning Approach for Predicting Defluorination of Per- and Polyfluoroalkyl Substances (PFAS) for Their Efficient Treatment and Removal. *Env. Sci. Techno. Lett.* **2019**, *6*, 624–629.
- (33) Nayak, S. K.; Yamijala, S. S. Computing accurate bond dissociation energies of emerging per- and polyfluoroalkyl substances: Achieving chemical accuracy using connectivity-based hierarchy schemes. *J. Hazard. Mater.* **2024**, *468*, 133804.
- (34) Zhang, P.; Wang, T.; Gong, J. Mechanistic Understanding of the Plasmonic Enhancement for Solar Water Splitting. *Adv. Mater.* **2015**, *27*, 5328–5342.
- (35) Yan, L.; Wang, F.; Meng, S. Quantum Mode Selectivity of Plasmon-Induced Water Splitting on Gold Nanoparticles. *ACS Nano* **2016**, *10*, 5452–5458.
- (36) Liu, L.; Zhang, X.; Yang, L.; Ren, L.; Wang, D.; Ye, J. Metal nanoparticles induced photocatalysis. *National Sci. Review* **2017**, *4*, 761–780.
- (37) Zhang, Y.; Chen, D.; Meng, W.; Li, S.; Meng, S. Plasmon-Induced Water Splitting on Ag-Alloyed Pt Single-Atom Catalysts. *Front. Chemistry* **2021**, *9*, 742794.
- (38) Feng, Q.; Zhang, Y.; Feng, H.; Liu, D.; Li, Q. Photocatalytic water splitting in the gap between plasmonic gold nanoclusters. *Phys. Fluids* **2023**, *35*, 073334.
- (39) Mukherjee, S.; Libisch, F.; Large, N.; Neumann, O.; Brown, L. V.; Cheng, J.; Lassiter, J. B.; Carter, E. A.; Nordlander, P.; Halas, N. J. Hot Electrons Do the Impossible: Plasmon-Induced Dissociation of H<sub>2</sub> on Au. *Nano Lett.* **2013**, *13*, 240–247.
- (40) Mukherjee, S.; Zhou, L.; Goodman, A. M.; Large, N.; Ayala-Orozco, C.; Zhang, Y.; Nordlander, P.; Halas, N. J. Hot-Electron-Induced Dissociation of H<sub>2</sub> on Gold Nanoparticles Supported on SiO<sub>2</sub>. *J. Am. Chem. Soc.* **2014**, *136*, 64–67.
- (41) Yan, L.; Ding, Z.; Song, P.; Wang, F.; Meng, S. Plasmon-induced dynamics of H<sub>2</sub> splitting on a silver atomic chain. *App. Phys. Lett.* **2015**, *107*, 083102.
- (42) Zhou, L.; Zhang, C.; McClain, M. J.; Manjavacas, A.; Krauter, C. M.; Tian, S.; Berg, F.; Everitt, H. O.; Carter, E. A.; Nordlander, P.; Halas, N. J. Aluminum Nanocrystals as a Plasmonic Photocatalyst for Hydrogen Dissociation. *Nano Lett.* **2016**, *16*, 1478–1484.
- (43) Wu, Q.; Zhou, L.; Schatz, G. C.; Zhang, Y.; Guo, H. Mechanistic Insights into Photocatalyzed H<sub>2</sub> Dissociation on Au Clusters. *J. Am. Chem. Soc.* **2020**, *142*, 13090–13101.

- (44) Li, T. E.; Hammes-Schiffer, S. Nuclear-Electronic Orbital Quantum Dynamics of Plasmon-Driven H<sub>2</sub> Photodissociation. *J. Am. Chem. Soc.* **2023**, *145*, 18210–18214.
- (45) Robatjazi, H.; Zhao, H.; Swearer, D.; Hogan, N.; Zhou, L.; Alabastri, A.; McLain, M.; Nordlander, P.; Halas, N. Plasmon-induced selective carbon dioxide conversion on earth-abundant aluminum-cuprous oxide antenna-reactor nanoparticles. *Nat. Comm.* **2017**, *8*, 27.
- (46) Kumari, G.; Zhang, X.; Devasia, D.; Heo, J.; Jain, P. K. Watching Visible Light-Driven CO<sub>2</sub> Reduction on a Plasmonic Nanoparticle Catalyst. *ACS Nano* **2018**, *12*, 8330–8340.
- (47) Zhang, Y.; Yan, L.; Guan, M.; Chen, D.; Xu, Z.; Guo, H.; Hu, S.; Zhang, S.; Liu, X.; Guo, Z.; Li, S.; Meng, S. Indirect to Direct Charge Transfer Transition in Plasmon-Enabled CO<sub>2</sub> Photoreduction. *Adv. Science* **2022**, *9*, 2102978.
- (48) Hu, C.; Chen, X.; Low, J.; Yang, Y.-W.; Li, H.; Wu, D.; Chen, S.; Jin, J.; Li, H.; Ju, H.; Wang, C.-H.; Lu, Z.; Long, R.; Song, L.; Xiong, Y. Publisher Correction: Near-infrared-featured broadband CO<sub>2</sub> reduction with water to hydrocarbons by surface plasmon. *Nat. Comm.* **2023**, *14*, 1580.
- (49) Wei, Y.; Mao, Z.; Jiang, T.-W.; Li, H.; Ma, X.-Y.; Zhan, C.; Cai, W.-B. Uncovering Photoelectronic and Photothermal Effects in Plasmon-Mediated Electrocatalytic CO<sub>2</sub> Reduction. *Angew. Chem. Internat. Ed.* **2024**, *63*, e202317740.
- (50) Herring, C. J.; Montemore, M. M. Mechanistic Insights into Plasmonic Catalysis by Dynamic Calculations: O<sub>2</sub> and N<sub>2</sub> on Au and Ag Nanoparticles. *Chem. Mater.* **2023**, *35*, 1586–1593.
- (51) Puértolas, B.; Comesaña-Hermo, M.; Besteiro, L. V.; Vázquez-González, M.; Correa-Duarte, M. A. Challenges and Opportunities for Renewable Ammonia Production via Plasmon-Assisted Photocatalysis. *Adv. Energy Mater.* **2022**, *12*, 2103909.
- (52) Hu, C.; Chen, X.; Jin, J.; Han, Y.; Chen, S.; Ju, H.; Cai, J.; Qiu, Y.; Gao, C.; Wang, C.; Qi, Z.; Long, R.; Song, L.; Liu, Z.; Xiong, Y. Surface Plasmon Enabling Nitrogen Fixation in Pure Water through a Dissociative Mechanism under Mild Conditions. *J. Am. Chem. Soc.* **2019**, *141*, 7807–7814.
- (53) Martinez, J. M. P.; Carter, E. A. Prediction of a low-temperature N<sub>2</sub> dissociation catalyst exploiting near-IR-to-visible light nanoplasmatics. *Science Advances* **2017**, *3*, eaao4710.
- (54) Brongersma, M.; Halas, N.; Nordlander, P. Plasmon-induced hot carrier science and technology. *Nat. nanotech.* **2015**, *10*, 25–34.
- (55) Rossi, T. P.; Erhart, P.; Kuisma, M. Hot-Carrier Generation in Plasmonic Nanoparticles: The Importance of Atomic Structure. *ACS Nano* **2020**, *14*, 9963–9971.
- (56) Linic, S.; Christopher, P.; Ingram, D. Plasmonic-metal nanostructures for efficient conversion of solar to chemical energy. *Nat. Mater.* **2011**, *10*, 911–21.
- (57) Boerigter, C.; Aslam, U.; Linic, S. Mechanism of Charge Transfer from Plasmonic Nanostructures to Chemically Attached Materials. *ACS Nano* **2016**, *10*, 6108–6115.
- (58) Boerigter, C.; Campana, R.; Morabito, M.; Linic, S. Evidence and implications of direct charge excitation as the dominant mechanism in plasmon-mediated photocatalysis. *Nat. Comm.* **2016**, *7*, 10545.
- (59) Ostovar, B.; Lee, S. A.; Mehmood, A.; Farrell, K.; Searles, E. K.; Bourgeois, B.;

- Chiang, W.-Y.; Misiura, A.; Gross, N.; Al-Zubeidi, A.; Dionne, J. A.; Landes, C. F.; Zanni, M.; Levine, B. G.; Link, S. The role of the plasmon in interfacial charge transfer. *Science Advances* **2024**, *10*, eadp3353.
- (60) Aslam, U.; Rao, V.; Chavez, S.; Linic, S. Catalytic conversion of solar to chemical energy on plasmonic metal nanostructures. *Nat. Catalysis* **2018**, *1*, 656–665.
- (61) Kumar, P. V.; Rossi, T. P.; Marti-Dafcik, D.; Reichmuth, D.; Kuisma, M.; Erhart, P.; Puska, M. J.; Norris, D. J. Plasmon-Induced Direct Hot-Carrier Transfer at Metal–Acceptor Interfaces. *ACS Nano* **2019**, *13*, 3188–3195.
- (62) Feng, Q.; Zhang, Y.; Feng, H.; Liu, D.; Li, Q. Evidence of Direct Charge Transfer in Plasmon-Mediated Photocatalytic Water Splitting: A Time-Dependent Density Functional Theory Study. *Phys. Fluids* **2022**, *34*, 113323.
- (63) Golubev, A. A.; Khlebtsov, B. N.; Rodriguez, R. D.; Chen, Y.; Zahn, D. R. T. Plasmonic Heating Plays a Dominant Role in the Plasmon-Induced Photocatalytic Reduction of 4-Nitrobenzenethiol. *J. Phys. Chem. C* **2018**, *122*, 5657–5663.
- (64) Jain, P. K. Taking the Heat Off of Plasmonic Chemistry. *J. Phys. Chem. C* **2019**, *123*, 24347–24351.
- (65) Elias, R. C.; Linic, S. Elucidating the Roles of Local and Nonlocal Rate Enhancement Mechanisms in Plasmonic Catalysis. *J. Am. Chem. Soc.* **2022**, *144*, 19990–19998.
- (66) Elias, R. C.; Yan, B.; Linic, S. Probing Spatial Energy Flow in Plasmonic Catalysts from Charge Excitation to Heating: Nonhomogeneous Energy Distribution as a Fundamental Feature of Plasmonic Chemistry. *J. Am. Chem. Soc.* **2024**, *146*, 29656–29663.
- (67) Ratchford, D. C. Plasmon-Induced Charge Transfer: Challenges and Outlook. *ACS Nano* **2019**, *13*, 13610–13614.
- (68) Zhang, Y.; Chen, D.; Meng, W.; Xu, Z.; Guo, H.; Li, S.; Meng, S. Plasmon-Mediated CO<sub>2</sub> Photoreduction via Indirect Charge Transfer on Small Silver Nanoclusters. *J. Phys. Chem. C* **2021**, *125*, 26348–26353.
- (69) Zhou, L.; Huang, Q.; Xia, Y. Plasmon-Induced Hot Electrons in Nanostructured Materials: Generation, Collection, and Application to Photochemistry. *Chem. Reviews* **2024**, *124*, 8597–8619.
- (70) Christopher, P.; Moskovits, M. Hot Charge Carrier Transmission from Plasmonic Nanostructures. *Ann. Rev. Phys. Chem.* **2017**, *68*, 379–398.
- (71) Zhang, Z.; Zhang, C.; Zheng, H.; Xu, H. Plasmon-Driven Catalysis on Molecules and Nanomaterials. *Acc. Chem. Research* **2019**, *52*, 2506–2515.
- (72) Kazuma, E.; Jung, J.; Ueba, H.; Treanary, M.; Kim, Y. Real-space and real-time observation of a plasmon-induced chemical reaction of a single molecule. *Science* **2018**, *360*, 521–526.
- (73) Kumar, P. V.; Rossi, T. P.; Marti-Dafcik, D.; Reichmuth, D.; Kuisma, M.; Erhart, P.; Puska, M. J.; Norris, D. J. Plasmon-Induced Direct Hot-Carrier Transfer at Metal–Acceptor Interfaces. *ACS Nano* **2019**, *13*, 3188–3195.
- (74) Rossi, T. P.; Kuisma, M.; Puska, M. J.; Nieminen, R. M.; Erhart, P. Kohn–Sham Decomposition in Real-Time Time-Dependent Density-Functional Theory: An Efficient Tool for Analyzing Plasmonic Excitations. *J. Chem. Th. Comp.* **2017**, *13*, 4779–4790.
- (75) Verma, P. K.; Kumar, V. B.; Srinivasan, V. Plasmon Induced Charge Transfer Dynamics in Metallic Nanoparticle-

- MoSe<sub>2</sub> Nanoflake Heterostructures. *Adv. Opt. Mater.* **2025**, *13*, 2402679.
- (76) Giesecking, R. L. M. Plasmons: untangling the classical, experimental, and quantum mechanical definitions. *Mater. Horiz.* **2022**, *9*, 25–42.
- (77) *Frontiers of Plasmon Enhanced Spectroscopy, Volume 1*; ACS Symposium Series; American Chemical Society: Washington, DC, 2016; Vol. 1245.
- (78) Kumar, P. V.; Rossi, T. P.; Kuisma, M.; Erhart, P.; Norris, D. J. Direct hot-carrier transfer in plasmonic catalysis. *Faraday Discuss.* **2019**, *214*, 189–197.
- (79) Fusco, Z.; Koenig, D.; Smith, S. C.; Beck, F. J. Ab initio investigation of hot electron transfer in CO<sub>2</sub> plasmonic photocatalysis in the presence of hydroxyl adsorbate. *Nanosc. Horiz.* **2024**, *9*, 1030–1041.
- (80) Yamijala, S. S. R. K. C.; Shinde, R.; Wong, B. M. Real-time degradation dynamics of hydrated per- and polyfluoroalkyl substances (PFASs) in the presence of excess electrons. *Phys. Chem. Chem. Phys.* **2020**, *22*, 6804–6808.
- (81) Ali, Z. A.; Yamijala, S. S.; Wong, B. M. A review of emerging photoinduced degradation methods for per- and polyfluoroalkyl substances in water. *Current Opini. Chem. Eng.* **2023**, *41*, 100947.
- (82) Biswas, S.; Yamijala, S. S. R. K. C.; Wong, B. M. Degradation of Per- and Polyfluoroalkyl Substances with Hydrated Electrons: A New Mechanism from First-Principles Calculations. *Env. Sci. Technology* **2022**, *56*, 8167–8175.
- (83) Yamijala, S. S.; Shinde, R.; Hanasaki, K.; Ali, Z. A.; Wong, B. M. Photo-induced degradation of PFASs: Excited-state mechanisms from real-time time-dependent density functional theory. *J. Hazard. Mater.* **2022**, *423*, 127026.
- (84) Perdew, J. P.; Burke, K.; Ernzerhof, M. Generalized Gradient Approximation Made Simple. *Phys. Rev. Lett.* **1996**, *77*, 3865–3868.
- (85) Mortensen, J. J.; Hansen, L. B.; Jacobsen, K. W. Real-space grid implementation of the projector augmented wave method. *Phys. Rev. B* **2005**, *71*, 035109.
- (86) Enkovaara, J. et al. Electronic structure calculations with GPAW: a real-space implementation of the projector augmented-wave method. *J. Phys.: Condens. Matter* **2010**, *22*, 253202.
- (87) Larsen, A. H. et al. The atomic simulation environment—a Python library for working with atoms. *J. Phys. Cond. Matter* **2017**, *29*, 273002.
- (88) Pfrommer, B. G.; Côté, M.; Louie, S. G.; Cohen, M. L. Relaxation of Crystals with the Quasi-Newton Method. *J. Computat. Phys.* **1997**, *131*, 233–240.
- (89) Larsen, A. H.; Vanin, M.; Mortensen, J. J.; Thygesen, K. S.; Jacobsen, K. W. Localized atomic basis set in the projector augmented wave method. *Phys. Rev. B* **2009**, *80*, 195112.
- (90) Kuisma, M.; Ojanen, J.; Enkovaara, J.; Rantala, T. T. Kohn-Sham potential with discontinuity for band gap materials. *Phys. Rev. B* **2010**, *82*, 115106.
- (91) Gritsenko, O.; van Leeuwen, R.; van Lenthe, E.; Baerends, E. J. Self-consistent approximation to the Kohn-Sham exchange potential. *Phys. Rev. A* **1995**, *51*, 1944–1954.
- (92) Humphrey, W.; Dalke, A.; Schulten, K. VMD: visual molecular dynamics. *J. Mol. Graph.* **1996**, *14*, 33.
- (93) Momma, K.; Izumi, F. VESTA 3 for three-dimensional visualization of crystal, volumetric and morphology data. *J. Appl. Cryst.* **2011**, *44*, 1272.

- (94) Harris, C. R. et al. Array programming with NumPy. *Nature* **2020**, *585*,, 357.

# TOC Graphic

